Data Mine

The CIELO Seismic Experiment

Heather A. Ford*[1], Maximiliano J. Bezada[2], Joseph S. Byrnes[2,3], Andrew Birkey[1], and Zhao Zhu[2]

Abstract

The Crust and lithosphere Investigation of the Easternmost expression of the Laramide Orogeny was a two-year deployment of 24 broadband, compact posthole seismometers in a linear array across the eastern half of the Wyoming craton. The experiment was designed to image the crust and upper mantle of the region to better understand the evolution of the cratonic lithosphere. In this article, we describe the motivation and objectives of the experiment; summarize the station design and installation; provide a detailed accounting of data completeness and quality, including issues related to sensor orientation and ambient noise; and show examples of collected waveform data from a local earthquake, a local mine blast, and a teleseismic event. We observe a range of seasonal variations in the long-period noise on the horizontal components (15–20 dB) at some stations that likely reflect the range of soil types across the experiment. In addition, coal mining in the Powder River basin creates high levels of short-period noise at some stations. Preliminary results from *Ps* receiver function analysis, shear-wave splitting analysis, and averaged *P*-wave delay times are also included in this report, as is a brief description of education and outreach activities completed during the experiment.

Cite this article as Ford, H. A., M. J. Bezada, J. S. Byrnes, A. Birkey, and Z. Zhu (2021). The CIELO Seismic Experiment, *Seismol. Res. Lett.* **93**, 1063–1074, doi: 10.1785/0220210237.

Supplemental Material

Introduction

The Crust and lithosphere Investigation of the Easternmost expression of the Laramide Orogeny (CIELO) was a two-year pilot experiment that deployed a linear array of 24 broadband, compact posthole (PH) seismometers spanning the Powder River basin in eastern Wyoming, extending from the southernmost Bighorn Mountains to the west and through to the Black Hills in South Dakota to the east (Fig. 1). The goal of the project was to better image the structure of the crust and lithospheric mantle of the eastern half of the Wyoming craton.

The Wyoming craton is an Archean craton located primarily in Wyoming, but it is also thought to extend into westernmost South Dakota, large portions of Montana, and easternmost Idaho (e.g., Whitmeyer and Karlstrom, 2007). The craton is subdivided into three regions, based on distinctive variations in age, isotopic signature, and lower crust seismic signatures (Mueller and Frost, 2006) and is thought to have stabilized by the late Archean. The craton accreted to greater Laurentia at 1.8–1.9 Ga (Mueller and Frost, 2006) and then became tectonically quiescent through the remainder of the Proterozoic and into the Late Cretaceous. During the Laramide orogeny, the Wyoming craton experienced significant tectonic deformation, with 50–60 km of crustal shortening accommodated by thrusting (Bird, 1998) that resulted in a series of basement-cored uplifts including, but not limited to, the Wind River Range, Laramie Range, and Bighorn Mountains. In the northern United States, the Black Hills mark the most physiographically pronounced Laramide associated uplift east of the Rocky Mountains (Tikoff and Maxson, 2001).

A common characteristic of cratons is their thick lithospheric mantle keels, which can extend to depths of 200 km or greater (Clouzet *et al.*, 2018). These thickened keels are thought to be convectively stable despite their cold temperatures in part because of a positive chemical buoyancy (Jordan, 1978; Lee, 2006) likely the result of melt depletion processes (Pollack, 1986). Importantly, the cold and neutrally buoyant mantle of cratons is thought to make cratons mechanically strong and capable of withstanding tectonic modification, with a few notable exceptions (Bedle *et al.*, 2021). The current generation of tomographic models for the Wyoming craton do not agree as to the depth extent of the lithospheric keel. Body-wave models image a region of high-velocity material extending to depths of 250 km beneath our study area in eastern Wyoming (Schmandt and Humphreys, 2010; Schmandt and Lin, 2014; Wang *et al.*, 2016), whereas some surface-wave models (Dave and Li, 2016) show high velocities possibly terminating at shallower depths. One interpretation of

1. Department of Earth and Planetary Sciences, University of California—Riverside, Riverside, California, U.S.A., https://orcid.org/0000-0002-3278-962X (AB); 2. Department of Earth and Environmental Sciences, University of Minnesota, Twin Cities, Minneapolis, Minnesota, U.S.A., https://orcid.org/0000-0002-6161-399X (JSB); https://orcid.org/0000-0003-4837-8689 (ZZ); 3. Now at School of Earth and Sustainability, Northern Arizona University, Flagstaff, Arizona, U.S.A.

*Corresponding author: heather.ford@ucr.edu

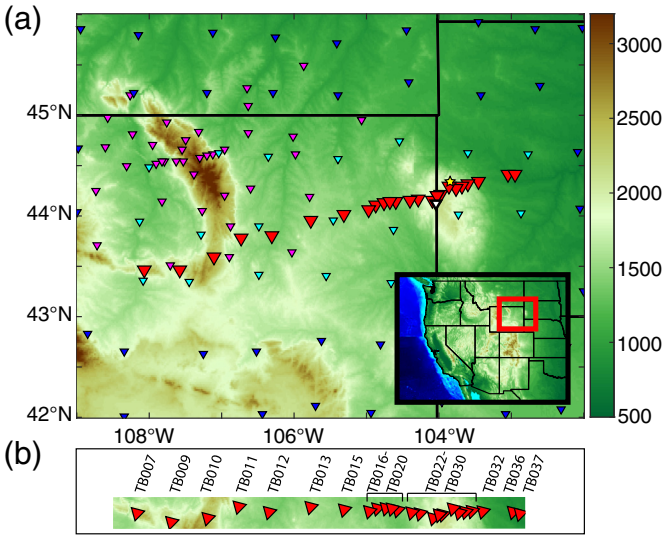

Figure 1. (a) Station map of the Crust and lithosphere Investigation of the Easternmost expression of the Laramide Orogeny (CIELO) seismic experiment. CIELO stations (2 F) are shown as red inverted triangles. Transportable Array (TA) stations are shown as blue and cyan inverted triangles, and Bighorn Arch Seismic Experiment (XV) broadband stations are shown as magenta inverted triangles. The geographic center of the Homestake Array (X6) is shown as a yellow star. Permanent station RSSD (IU) is shown as a small white inverted triangle. Color bar corresponds to elevation (in meters). Inset map shows regional topography with the red box indicating location shown in (a). (b) CIELO alphanumeric station names, with numbering that increases from west to east. The color version of this figure is available only in the electronic edition.

the deepest high-velocity feature is that it represents the depleted Shatsky conjugate, which subcreted to the base of the cratonic lithosphere during subduction of the Farallon slab (Humphreys *et al.*, 2015). Alternatively, the high velocities may represent active downwelling of the Wyoming craton destabilized through a combination of flat slab subduction, small-scale convection, and hotspot activity in western Wyoming (Dave and Li, 2016). It is also possible that it represents anomalously thick and intact lithosphere, original to the craton.

The goal of the CIELO experiment is to advance our understanding of the processes that modify, destroy, and possibly rebuild the cratonic lithosphere by investigating the structure of the Wyoming craton. In particular, we aim to clarify the dimensions of the thickest part of its lithospheric keel, which we refer to as the Thunder Basin Block, to understand if such a feature could represent a stable rigid block (whether original or allochthonous to the Archean craton) or a weakened remnant in the process of delamination. A second objective is to explore the relationship of the Thunder Basin Block to Laramide basement-involved thrusting in the Black Hills and to better characterize the location of the eastern edge of the Wyoming craton, the location of which has recently been debated (Kilian *et al.*, 2016; Worthington *et al.*, 2016).

Future seismic imaging studies will use data collected from the CIELO experiment in addition to data from the EarthScope Transportable Array (TA) and other temporary and flexible array experiments, including the Bighorn Arch Seismic Experiment (BASE) (network XV) and the Homestake Array (X6) (Mandic *et al.*, 2018). The only permanent station located within the study area is station RSSD (IU), located within the Black Hills (Fig. 1). Crustal thickness will primarily be constrained by *Ps* receiver function analysis (see the Initial Observations and Results section). Better constraints on the geometry and physical properties of the upper mantle beneath eastern Wyoming will come from *Sp* receiver function analysis, body-wave tomography, surface-wave tomography, and body-wave attenuation. Shear-wave splitting observations will look for evidence of allochthonous and/or downwelling lithosphere as well as changes associated with the craton margin. Finally, a seismicity catalog will be constructed to test the hypothesis that deformation is concentrated along the edges of the Thunder Basin Block, as has been observed in other intraplate settings (Bezada, 2017; Bezada and Smale, 2019).

Instrumentation and Deployment

The CIELO seismic array, shown in Figure 1, consisted of 24 broadband seismic stations, distributed in a linear array with station spacing between 4 and 47 km, with an average spacing interval of 19 km. In general, stations along the western half of the array were spaced further apart, whereas stations in the eastern half of the array crossing into the Black Hills were more densely spaced with an average spacing of 10 km. The decision to decrease the average station spacing from west to east was made to maximize limited project resources. The earlier BASE deployment ensured overlapping coverage along the western half of the array and allowed us to densify the array in the eastern half, where tomography suggests the eastern margin of the Thunder Basin Block is located (Humphreys *et al.*, 2015). Additional variations in interstation spacing were the result of landowner permission. All stations were installed on private property, primarily ranch land, with permission from the landowner and were accessible with a well-equipped four-wheel drive vehicle. The primary physiographic features sampled by the array included the Owl Creek Mountains, a Laramide uplift that extends westward from the southern margin of the Bighorn Mountains, the Powder River basin, and the Black Hills. Instruments were installed in September 2017, and service runs to check on instrument condition were carried out in March and September 2018. The instruments were removed in September 2019. The location of the array was selected to target the Black Hills, the high-velocity region (Thunder Basin Block) imaged in previous studies (e.g., Humphreys *et al.*, 2015) and to cross the inferred contact between the Wyoming craton and Trans-Hudson orogen (Kilian *et al.*, 2016; Worthington *et al.*, 2016).

Instrumentation for the CIELO experiment consisted of Nanometrics Meridian Compact PH seismometers provided

by collaborators M. Bezada and H. Ford. The use of direct-burial PH sensors has become increasingly popular in recent years, in large part due to the ease of deployment (e.g., Tape *et al.*, 2017). The Meridian Compact PH utilizes the same sensor as the Trillium compact, but also houses the digitizer within the same case. This arrangement results in a quicker and more streamlined installation process, important for limited-budget pilot experiments such as the one described here. The Meridian Compact PH seismometers are sensitive to periods of up to 120 s, and data for the experiment were recorded on three channels at a rate of 100 samples per second. The sensors were installed via direct burial to a depth of three feet, uncased (Bezada *et al.*, 2019), and reburied with the original soil, with no additional materials or sands added. The bottom surface of the hole was flattened with the end of a large dowel, and the sensor was installed to level. As the sensor was reburied, it was tightly packed with original soil (again using the dowel), and tilt was checked repeatedly. It should be noted that the Meridian Compact PH does not have a self-leveling feature and that well-centered masses will provide the best noise performance; therefore, care was taken to ensure accurate leveling during installation.

The stations were equipped with solar panels and power boxes provided by the Incorporated Research Institutions for Seismology–Program for the Array Seismic Studies of the Continental Lithosphere (IRIS-PASSCAL) instrument center. Solar panel mounts provided by IRIS were used to support the solar panels and were stabilized with additional stakes and wiring. A single deep cycle marine battery was used at each station. Beneath the mount, a 24-gal Rubbermaid Action Packer was installed to house the solar controller box, battery, and Surface Interface Unit (SIU). The SIU connects to the buried sensor and provides display information about the status of Global Positioning System, power, and sensor; provides data storage (removable memory card in a waterproof cartridge); and allows users to connect a tablet or computer (via Ethernet cable) to interface with the instrument and conduct a more detailed state of health assessment. The action packer was buried (with the top approximately one-fifth exposed) to provide some thermal regulation. The action packer was then covered with a tarp and additional soil. Barbed wire fencing was placed around most stations to prevent cattle from disturbing the installation, and heavy-duty guard rails were installed at select sites at the request of landowners. See Figure S1, available in the supplemental material to this article, for a photographic example of an installed station.

TABLE 1
Station Names, Latitudes, and Longitudes, Calculated Data Availability (IRIS MUSTANG), and misorientation (IRIS LASSO)

Station	Latitude	Longitude	Percent Availability	Misorientation
TB007	43.4684	−108.0647	100	1.3
TB009	43.4626	−107.5816	100	7.5
TB010	43.5906	−107.1082	99.99	−0.8
TB011	43.7841	−106.7262	99.99	0.4
TB012	43.8090	−106.3106	100	2.4
TB013	43.9543	−105.7656	87.13	9.2
TB015	44.0188	−105.3095	90.48	4.8
TB016	44.0614	−104.9750	100	1.8
TB017	44.1080	−104.8755	99.86	9.6
TB018	44.1354	−104.7575	99.97	8.2
TB019	44.1489	−104.6827	100	0.1
TB020	44.1380	−104.5986	99.98	3.6
TB022	44.1504	−104.3981	99.97	6.3
TB023	44.1645	−104.2919	77.75	5.0
TB024	44.1501	−104.0908	73.16	2.0
TB025	44.2066	−104.0264	99.6	3.6
TB026	44.2125	−103.9773	100	20.8
TB027	44.3001	−103.8690	99.74	6.4
TB028	44.2764	−103.7605	99.97	−5.9
TB029	44.2979	−103.6861	100	24.3
TB030	44.3249	−103.5995	99.97	15.0
TB032	44.3386	−103.4508	100	10.2
TB036	44.4089	−103.0495	100	8.6
TB037	44.4183	−102.9543	83.57	16.9

IRIS LASSO, Incorporated Research Institutions for Seismology Latest Assessment of Seismic Station Observations; IRIS MUSTANG, Incorporated Research Institutions for Seismology Modular Utility for STAtistical kNowledge Gathering system.

Data Availability and Quality

The percent data availability as measured by the IRIS Modular Utility for STAtistical kNowledge Gathering system (MUSTANG) (see Data and Resources) shows that for most stations the availability approaches 100%, with 19 of the 24 stations in our network having a percent data availability exceeding 99.5% (Table 1). Of the remaining five stations, all exceeded 70% data availability. Station TB013 experienced an outage during the last three months of the deployment due to an improperly formatted memory card. Memory card issues also resulted in a gap in data from July to September 2018 at stationTB015. At station TB037, power was lost in May 2019 due to a cut solar panel cable because an animal appeared to have chewed through the power cable. At stations TB023 and TB024, the gaps in data were not immediately explainable, for the sites and equipment were undisturbed, making the most plausible explanation power-related. Table 1 lists the percent

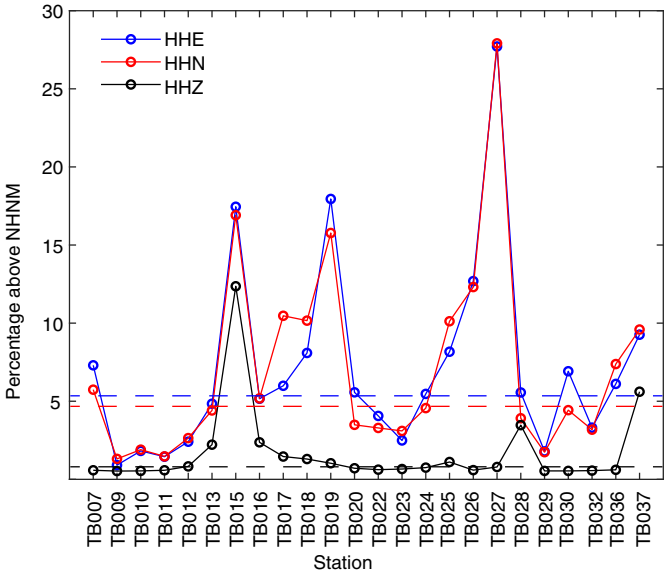

Figure 2. Mean percentage of probability density function (PDF) values, at each station, that exceed the Peterson New High Noise Model (NHNM) from 1 October 2017 to 15 September 2019 for the HHE (blue), HHN (red), and HHZ (black) components of the CIELO seismic array. The median values among all stations for each component are shown with horizontal dashed lines. A detailed discussion of the peaks in noise can be found in the Data Availability and Quality section. The color version of this figure is available only in the electronic edition.

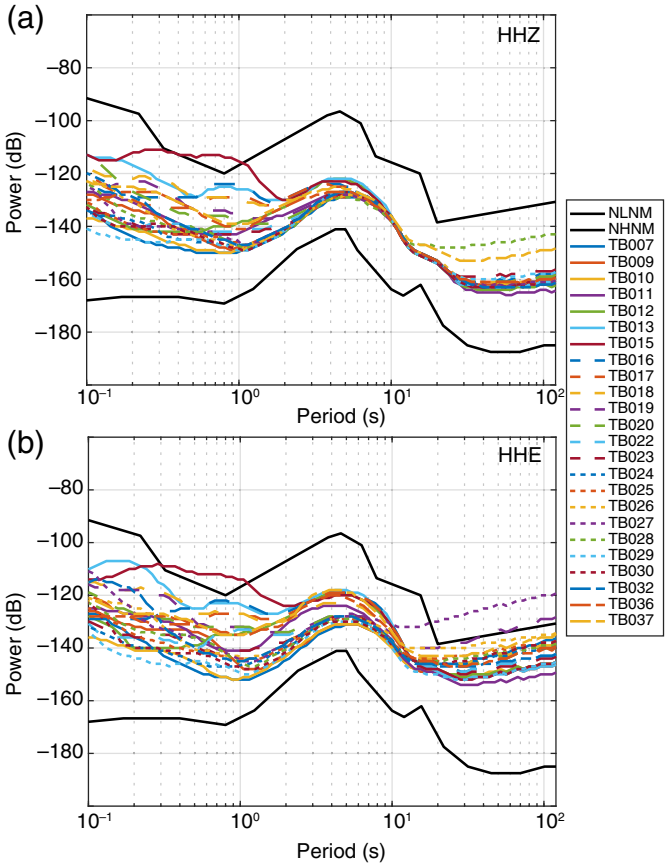

Figure 3. Seismic noise comparison using the mean value of PDFs for (a) HHZ and (b) HHE components for CIELO seismic stations. The NHNM and New Low Noise Model are both shown as thick, solid black lines. The color version of this figure is available only in the electronic edition.

data availability for each station. The waveform data are currently archived at the IRIS Data Management Center (DMC; see Data and Resources).

Utilizing the "orientation_check" function available from IRIS's Latest Assessment of Seismic Station Observations (LASSO), we performed an analysis to determine the apparent accuracy of sensor orientations recorded in the metadata. The LASSO's "orientation_check" function utilizes the Rayleigh-wave polarization of large ($M_w > 7.0$), shallow (<100 km depth) events to predict event back azimuths and then compares these to metadata-derived back azimuths (Stachnik *et al.*, 2012). The averaged misorientations for each station (assuming the 24-month experiment duration) are listed in Table 1. The average misorientation among all stations was 6.7°. Of the 24 stations, 12 were within ±5° and 19 were within ±10°. The remaining five stations had misorientations ranging from 10.2° (TB032) to 24.3° (TB029). Installation conditions (poor weather, limited time, and visibility) were primarily responsible for the larger misorientations. Instrument orientations were also calculated for time increments ranging from 2 to 24 months. Almost all stations show consistent values calculated over the various time intervals, with small changes seen at 2–6 months and 10–16 months at many of the stations. However, four stations show large changes in orientation—TB011, TB023, TB028, and TB037 throughout the experiment duration (see Fig. S2). At stations TB011 and TB023, changes in the orientations are due to the stations being reinstalled six months into the experiment. Station TB023 was reinstalled because the instrument masses indicated that the sensor was tilted. Station TB011 was reinstalled at the request of the property owner. The changes in orientation for the remaining stations, TB028 and TB037, are less clear. It is possible that the estimates for the shorter time increments may be inaccurate due to the limited number of events used in LASSO. In addition, increased ambient noise within the period band used in the Rayleigh-wave polarization calculations (25–50 s for LASSO calculations) can lead to mismeasurement (Stachnik *et al.*, 2012). Stations TB028 and TB037 are two of three stations with clearly elevated vertical-component noise (Fig. 2) and are the only stations with increased vertical-component noise observed at long periods (15–100 s) (Fig. 3). Although we are unable to confirm that this is the reason for the change in polarization direction with time, the explanation appears plausible.

Comparisons of ambient seismic noise between stations were completed using noise metrics provided by LASSO and MUSTANG, developed by IRIS using the methods

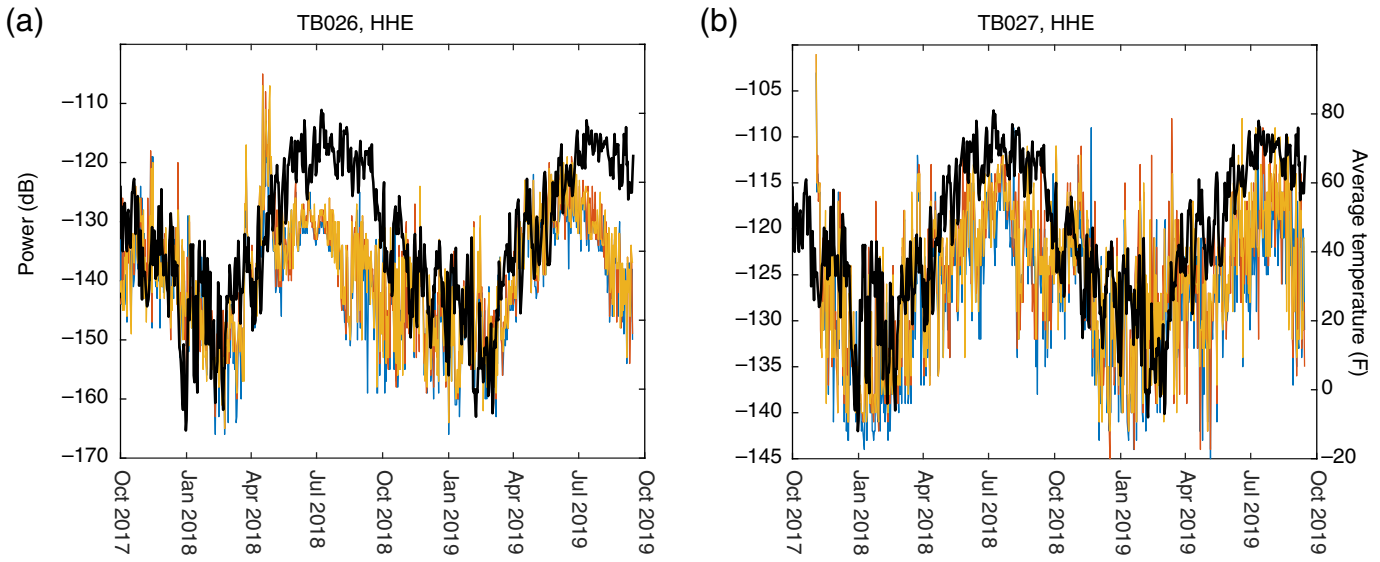

Figure 4. Plot of unfiltered daily power spectral density (PSD) values for (a) TB026.HHE and (b) TB027.HHE from installation to 15 September 2019 for three periods—43.6 s (blue), 51.9 s (red), and 61.7 s (orange). Superimposed on both panels is the average daily temperature at the Rapid City, South Dakota Regional Airport (black). An increase in long-period seismic noise is seen during the spring–summer months at both stations and may be related to the sandy clay soil in which both stations were installed. The color version of this figure is available only in the electronic edition.

described by McNamara and Buland (2004). We characterize the level of seismic noise by finding the mean percentage of probability density functions (PDFs) found above the Peterson New High Noise Model (NHNM) (Peterson, 1993) for a given time range. Using LASSO, we calculated the mean percentage of PDFs above the NHNM of the three components (HHE, HHN, and HHZ) for all 24 stations from 1 October 2017 to 15 September 2019. Figure 2 illustrates these percentages plotted by station. The median values for HHE, HHN, and HHZ among all stations in our array were 5.6%, 4.5%, and 0.7%, respectively. The quietest stations in our array, as defined by having all three component values at or below the median threshold calculated for all stations, are TB009, TB010, TB011, TB012, TB022, TB023, TB029, and TB032. The low-noise levels exhibited at stations TB009–TB012 are unsurprising, for they were located in an area with both low population and industrial and/or agricultural activity. Stations TB022 and TB023 were both located on ranches in a less remote but lightly populated region, whereas stations TB029 and TB032 were located on residential properties near paved roads.

Peaks in vertical-component noise are centered at stations TB015, TB028, and TB037. The peak at TB015 is particularly prominent in the 1–5 Hz band on the horizontal and vertical components (Fig. 3). We attribute this signal to a large active coal mine immediately adjacent to the property on which TB015 was installed, in the central Powder River basin. This noise tapers off quickly at stations adjacent to station TB015. Stations TB013 and TB016, located closest to TB015 at distances of ∼35 and ∼27 km, respectively, show significantly lower but still elevated levels of noise on the vertical component (Fig. 2).

Vertical-component noise is also moderately high at stations TB028 and TB037 (Fig. 2). At both stations, elevated mean PDF values at long periods are observed (Fig. 3). The cause of the noise at station TB037, which also has elevated levels of noise on the horizontal components (Figs. 3 and 4), is unclear. A heavy-duty cattle guard was installed at this site and may have produced noise in the wind, though other sites with similar guards were not as noisy. The station was located in a rural community well off of any paved road or other structures. Station TB028 was located adjacent to a sand and gravel processing facility, which may be the source of the noise observed at long periods.

Aside from station TB015, the largest peaks in noise are observed at stations TB019 and TB027 (Fig. 2). At these stations, along with adjacent stations TB018, TB025, and TB026, and to a lesser extent station TB017, horizontal noise levels are elevated relative to the median value of the network as a whole. As Figure 3 illustrates, horizontal noise levels at stations TB019 and TB027 are greatest at long periods. This long-period noise varies markedly with season for some stations. Unfiltered daily power spectral density (PSD) values for station TB027.HHE from installation to 15 September 2019 for three periods—43.6, 51.9, and 61.7 s are compared with the daily (unfiltered) average temperature at the Rapid City, South Dakota, Regional Airport in Figure 4. A clear correlation exists between the long-period noise and seasonal average temperature of the region. In the winter months, noise and temperature are at a minimum. In the spring, average temperatures and noise levels both rise, reaching a peak in July–August for both years. In total, an

approximate seasonal increase of ~15–20 dB is observed from winter to summer. A clear, positive correlation in temperature and noise levels is also observed at station TB026, again with a seasonal increase of ~20–25 dB (Fig. 4). At station TB026, the peak in noise appears offset, occurring slightly earlier in the season for both years of the deployment. At stations TB018, TB019, and TB025, some evidence of correlation to the seasonal trend exists over time periods of 3–6 months; however, the correlation is less clear than for stations TB026 and TB027, and the results are not shown here. Similar seasonal variations at long periods, with an increase of 10–20 dB from winter to summer, were observed at some vault-style stations in the Superior Province Rifting EarthScope Experiment (Wolin *et al.*, 2015). The seasonal variations were attributed to the material present at the stations, with stations buried in fine-grained silt and clay producing the largest changes in noise in response to atmospheric changes in pressure. We propose that a similar mechanism is responsible for the seasonal changes at stations TB026 and TB027, which were both installed in sandy clays. Stations TB018 and TB019, at which we also see some evidence for seasonal variability, were installed in bentonite.

Another useful noise comparison that we performed was to compare noise in our array to noise observed at TA stations located in our study area. To make the comparison, we once again used LASSO to calculate the mean percentage of PDFs above the NHNM at TA stations. The TA stations included in this analysis included H20A–H26A, I20–I26A, and J20A–J26A (cyan-colored station symbols in Fig. 1), and each mean percentage was calculated for the duration of station deployment for the BHE, BHN, and BHZ components. The median values for BHE, BHN, and BHZ among these stations are 2.58%, 2.73%, and 0.99%, respectively. When compared with the median values calculated for our array, the horizontal components from TA have moderately lower values, which we find consistent with the plotted PDFs for individual stations. As an example, we also directly compare PDFs from two stations, one from our array (TB024) and one from TA (I26A) (Fig. 5). These stations were selected because they both had a mean percentage of PDFs above the NHNM similar to the median calculated among all stations within their respective network. At longer periods (>20 s), the mean power of the PDFs for both the horizontal and vertical components of TB024 appears to be larger than for I26A. At short periods, the TA station appears noisier, possibly due to nearby anthropogenic noise sources. This analysis shows that the PH stations can record long- and short-period data of comparable quality to those from the much more labor-intensive vault designs used for the TA sites, though long periods are quieter at the TA station.

Initial Observations and Results

Teleseismic data and analysis

The majority of the proposed analyses for our experiment require the use of teleseismic event data. During the CIELO instrument deployment (1 October 2017–15 September 2019), there were 743 events of $M_w \geq 5.5$ that occurred within the epicentral distance range of 30°–120° (Fig. S3). Different analysis techniques require use of different subsets of this larger data set. For example, methods utilizing the direct *P* arrival, including *P*-wave tomography, *Ps* receiver function analysis, and *P*-wave attenuation, are limited to epicentral distances of 30°–90°, reducing the number of potential events to 272. To limit the effects of source-side attenuation, only events originating from depths greater than 250 km are considered when calculating *P*-wave attenuation, further limiting the pool to 20 potential events. For methods such as shear-wave splitting analysis, preliminary analysis at some stations shows that, of a pool of ~300 events, typically 30 measured splits and/or nulls are recorded. Aggregating the data recorded by CIELO, the TA, and the BASE experiments results in a joint dataset that suffices for our intended analyses; for example, Zhu *et al.* (2020) utilized approximately 1500 *P*-wave arrivals from 48 events for *P*-wave attenuation analysis, with 255 measurements from 11 events recorded by CIELO stations.

An example of averaged teleseismic SKS phase splitting results is shown in Figure 6 for stations TB012, TB019, and TB036. Initial observations suggest that both the polarization directions and splitting delay times vary along our array, consistent with earlier observations from other stations in the region as compiled from the SPUD database (see Data and Resources). Highly heterogeneous splitting directions were described by Anderson *et al.* (2014) utilizing data from the BASE array and were attributed to the presence of Archean lithosphere. One hypothesis that we intend to test is whether the changing fast wave polarization direction is related to the proposed eastern boundary of the Wyoming craton (Worthington *et al.*, 2016). If we confirm that splits west of station TB012 differ significantly and systematically from those east of station TB012, it may support the hypothesis that the eastern margin of the Wyoming craton is located immediately east of the Big Horn Mountains (Kilian *et al.*, 2016; Worthington *et al.*, 2016) rather than east of the Black Hills as is commonly shown (e.g., Whitmeyer and Karlstrom, 2007). Better understanding the location of the margin has the potential to improve our understanding of the Precambrian structure and evolution of North America and may help us to better understand why the Black Hills region accommodated deformation during the Laramide orogeny.

Local seismicity and the Powder River basin

Although the eastern half of the Wyoming craton is not currently experiencing any significant tectonic activity, low-magnitude seismicity does occur. A detailed six-month study of seismicity in the Bighorn Mountains and surrounding basins detected 89 earthquakes ranging in magnitude from $M_w - 0.5$ to 2.5 (O'Rourke *et al.*, 2016), including one located in the mantle at a depth of 63 km, with most seismicity occurring

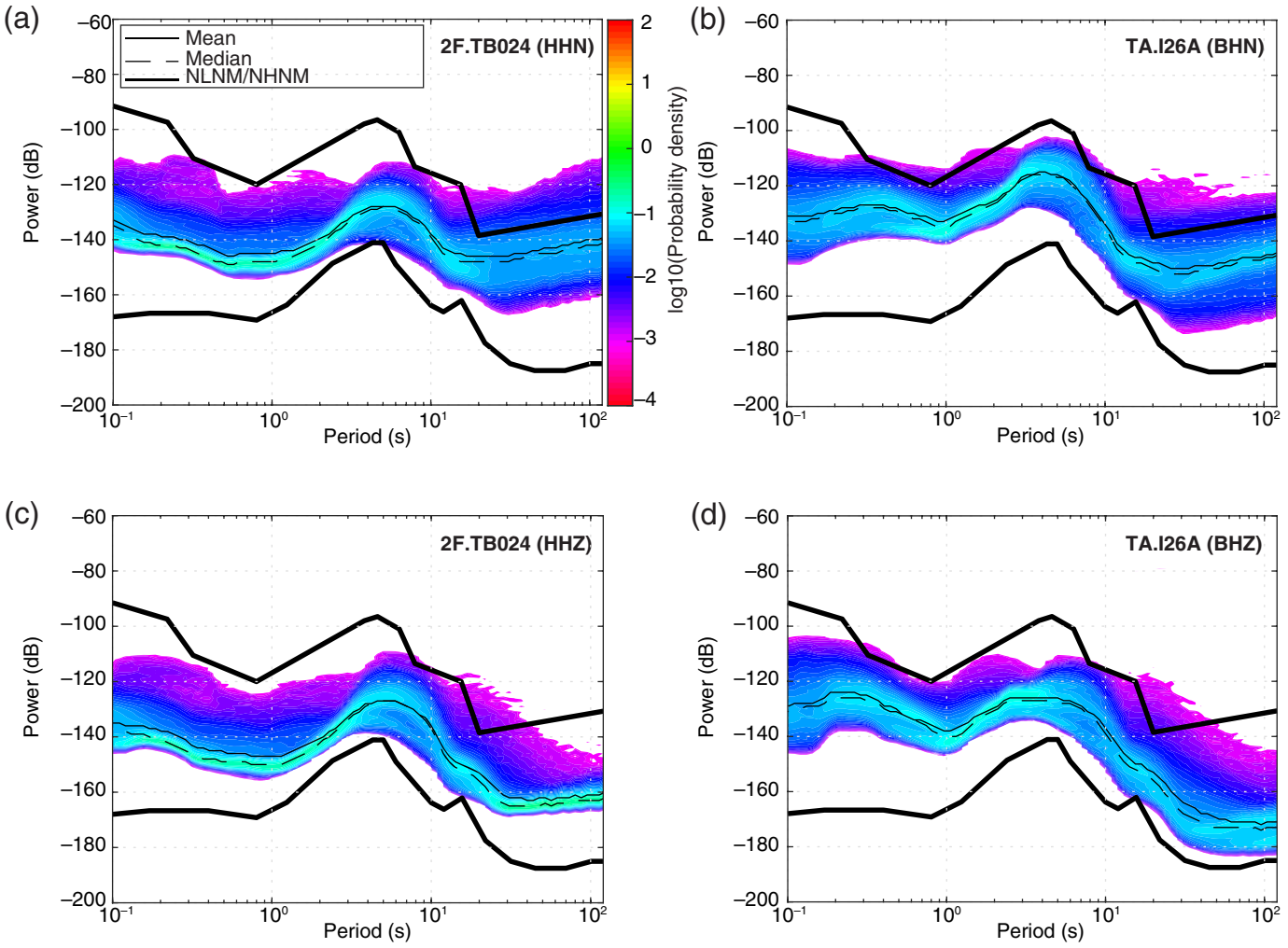

Figure 5. Seismic PDFs for (a,b) horizontal and (c,d) vertical components of (a,c) CIELO station TB024 (2 F), and (b,d) TA station I26A. Both stations exhibit similar mean noise values on the horizontal component at long periods, although the distributions are different. The (d) TA vertical component exhibits lower noise values at long periods than (c) TB024. At short periods, the (b,d) TA station appears noisier, likely due to nearby anthropogenic noise sources. The scale of the probability density is the same for (a–d) and corresponds to the color bar shown in (a). The color version of this figure is available only in the electronic edition.

in the high-topography regions of the Bighorn and Owl Creek Mountains. The authors propose that slip primary occurs as normal-faulting along pre-existing weaknesses created during the Laramide uplift, based on analysis of focal mechanisms.

The U.S. Geological Survey (USGS) Earthquake Catalog documents 14 earthquakes in our study area during the two years of the CIELO deployment, with magnitudes ranging from M_L 2.5 to M_w 4.0 (Fig. 7). The largest occurred in a one-week period from 31 October 2017 to 5 November 2017, when earthquakes of magnitude (in sequence) 2.6, 3.2, 4.0, 2.5, and 2.9 occurred within ~5 km of each other. A 300 s record of the M_w 4.0 event from our array is shown in Figure 8. This sequence occurred in the Owl Creek Mountains, in line with our array between stations TB009 and TB010 (Fig. 7). The calculated USGS moment tensor solution indicates that the M_w 4.0 event occurred along a normal fault, in agreement with earlier observations from the region in O'Rourke *et al.* (2016).

One of the overarching goals of our study is to better understand the relationship between the seismically imaged thick mantle lithosphere of the Wyoming craton and its potential role in transferring tectonic forces. To that end, we aim to leverage the increased seismic coverage to produce a detailed seismicity catalog with a lower magnitude of completeness. If the Thunder basin is acting as a rigid lithospheric block, we would expect to see seismicity around its periphery and not in its interior.

The Powder River basin, which our array transects between the Bighorn Mountains and the Black Hills, is a major coal producer. As a result of surface mining, large blasts are a common occurrence. During our experiment, the USGS Earthquake Catalog (see Data and Resources) recorded 428 M_L 2.5–3.9 mine

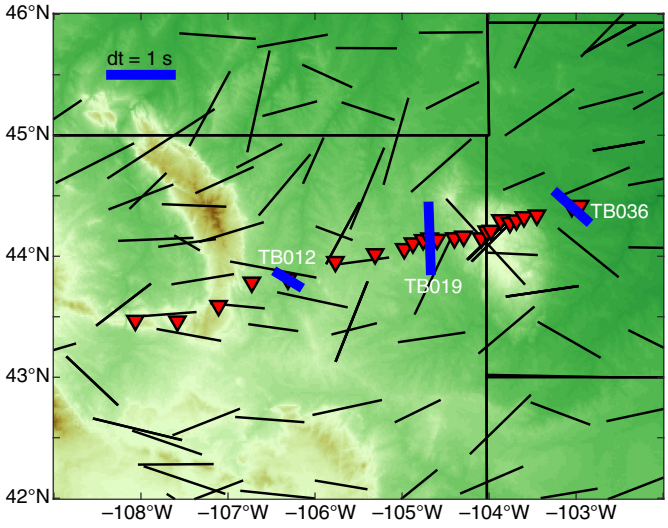

Figure 6. Map of shear-wave splitting results in which line length indicates delay time and line orientation indicates fast direction orientation. An example split with a delay time of 1 s and a fast direction of 90° is shown in the upper left corner. Black splits are from the SPUD database (see Data and Resources), and blue splits are the circular mean of splits calculated in Splitlab (Wüstefeld *et al.*, 2008) using the Rotation Correlation method (Bowman and Ando, 1987) and CIELO data for stations TB012, TB019, and TB036. The color version of this figure is available only in the electronic edition.

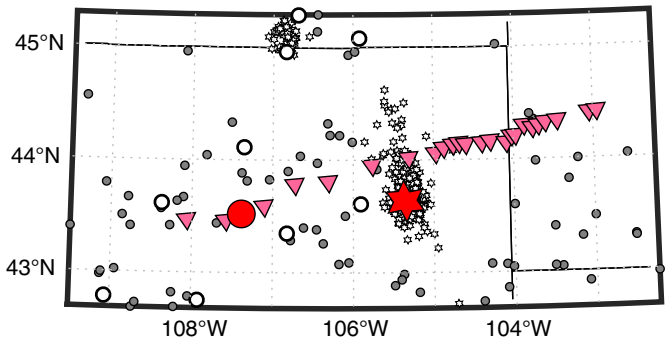

Figure 7. Overview of local seismicity, including mining blasts, in our general study area. Data were downloaded from the U.S. Geological Survey (USGS) Earthquake Catalog. Six years (August 2013–September 2019) of mine blasting events are shown with white stars. Roughly 30 yr of earthquake events (August 1990–September 2019) are shown as unfilled large circles (events occurring in the CIELO deployment, October 2017–September 2019) or smaller gray circles (events occurring prior to the CIELO deployment). Pink inverted triangles mark the location of CIELO seismic stations. Large red circle marks the approximate location of a sequence of five earthquakes that occurred 31 October 2017–5 November 2017, the largest of which was an *M* 4.0 and is shown in Figure 8. The large red star marks the location of a mine blast shown in Figure 8. The color version of this figure is available only in the electronic edition.

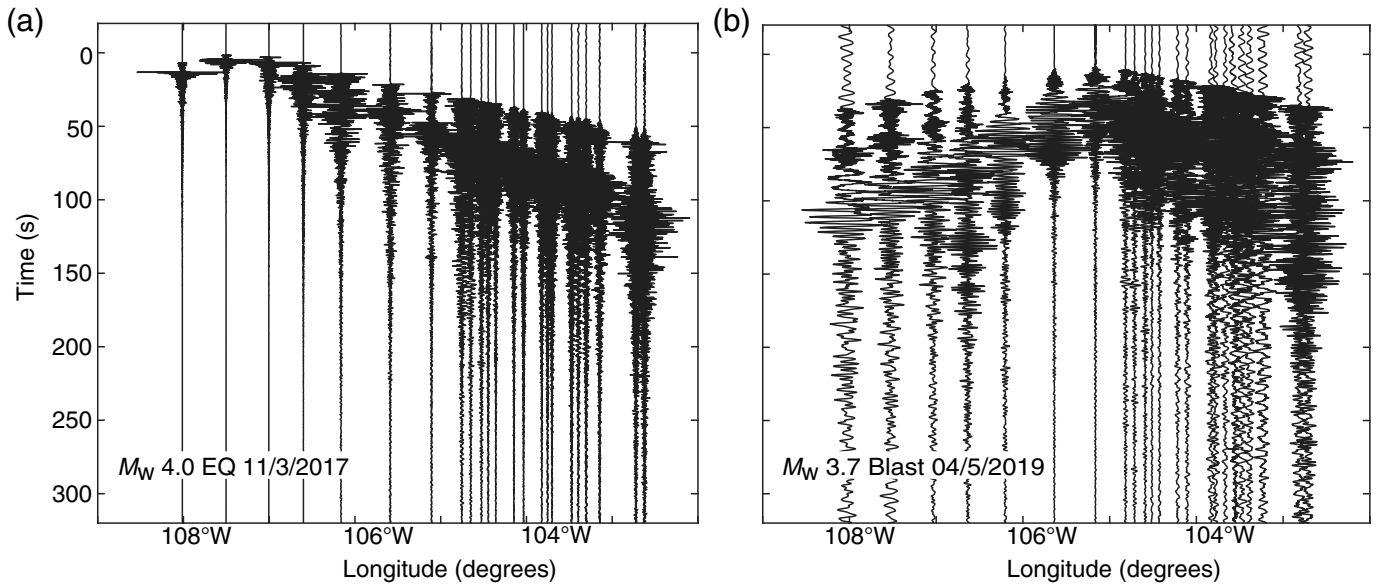

Figure 8. Vertical-component traces of local events recorded at CIELO seismic stations plotted as a function of longitude. (a) A local *M* 4.0 earthquake occurred on 3 November 2017 between stations TB009 and TB010 (Fig. 7). The earthquake was the largest local event to be recorded during the experiment and was preceded by at least two 2.5+ magnitude earthquakes and was followed by two additional 2.5+ magnitude earthquakes within a five-day period. (b) An example of a mine blast occurring slightly south of the array, nearest TB015 is also shown.

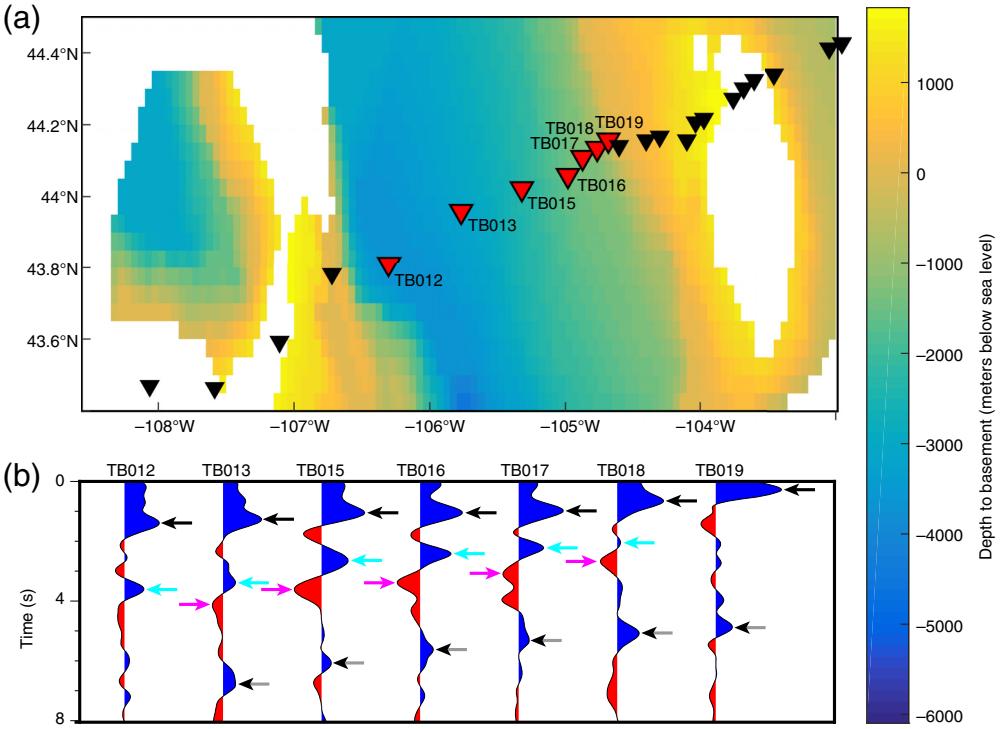

Figure 9. (a) Interpolated depth to basement from Blackstone (1993) with station locations superimposed. (b) *Ps* receiver functions calculated for a subset of stations within the CIELO seismic experiment. Black arrows correspond to the inferred *Ps* scattered phase from the sediment-basement contact, whereas cyan and magenta arrows are inferred to be the associated sediment multiples as determined from comparison of previously published forward modeled receiver functions (Yeck *et al.*, 2013). Gray arrows mark possible Moho scattered phase. Note that the receiver functions in the bottom panel are plotted equidistant from each other and do not reflect actual distances between stations. The color version of this figure is available only in the electronic edition.

blast events. The locations of these events are shown in Figure 7, and an example set of waveforms for a blast of M_L 3.7 is shown in Figure 8. The 425 events recorded by the USGS are likely a significant undercount given the lower magnitude threshold. O'Rourke *et al.* (2016) detected 1563 mining explosions in a six-month period (April 2010–September 2010) during the BASE, and Mandic *et al.* (2018) detected 359 explosions in a six-month window (July 2015–December 2015) during an experiment at the Homestake Mine in Lead, South Dakota. In Mandic *et al.* (2018), they noted that some mine explosion epicenters are poorly located, despite assuming fixed depth (surface mines with depth equal to zero). As part of our initial analysis, the boundaries of active coal mines in the Powder River basin were downloaded from the USGS online spatial data website and compared with the locations of mining explosion locations from 2012 to 2019, taken from the USGS Earthquake Catalog (see Data and Resources). Our initial analysis found that roughly 47% of mine explosions fall outside of the boundaries of active coal mines, suggesting that a considerable portion may be mislocated.

Accounting for the thick sedimentary sequence in the Powder River basin will be important for our work focused on deeper structure. Preliminary analysis of *Ps* receiver function shows the presence of significant scattered wave energy within the time window of 0–8 s (Fig. 9), much of which can be attributed to basin structure, including the contact between the basin and underlying basement rocks. For example, at station TB013, located above one of the thickest sections of the Powder River basin, a positive phase (corresponding to a velocity increase with increasing depth) is observed at 1.2 s, followed by a positive and negative phase couplet at 3.3/4.1 s. The first negative phase is interpreted to be the direct *Ps* phase originating from the interface between basin and basement, and the later positive and negative couplet is thought to be the arrival of the basin multiples. When compared with a forward model of scattered *Ps* phase arrival times from Yeck *et al.* (2013), the station TB013 arrival times agree with a basin depth of approximately 3.5 km. Although this is thinner than the ~4.5 km assumed from prior constraints of basin depth (Blackstone, 1993), potential differences between the assumed velocity model used in the forward modeling (Yeck *et al.*, 2013) and the actual velocity structure present in the basin, plus uncertainties in the basin depth map itself (Blackstone, 1993), suggest that our assumption that the phases represent basin-related seismic structure is reasonable. From stations TB012 to TB019, evidence of the basin-associated *Ps* scattered phases (and corresponding multiples) is observed and correlates well with basin depth (Fig. 9). For stations TB015–TB019, the estimated basin thickness determined by comparing our selected phases to the forward modeled receiver functions (Yeck *et al.*, 2013) agrees to within 0.5 km with the previously published basin depth map (Blackstone, 1993). At stations TB012 and TB013, the disagreement is ~1 km, and this can likely be attributed to differences between basin velocities and the assumed velocities in the forward model for the thickest parts of the basin.

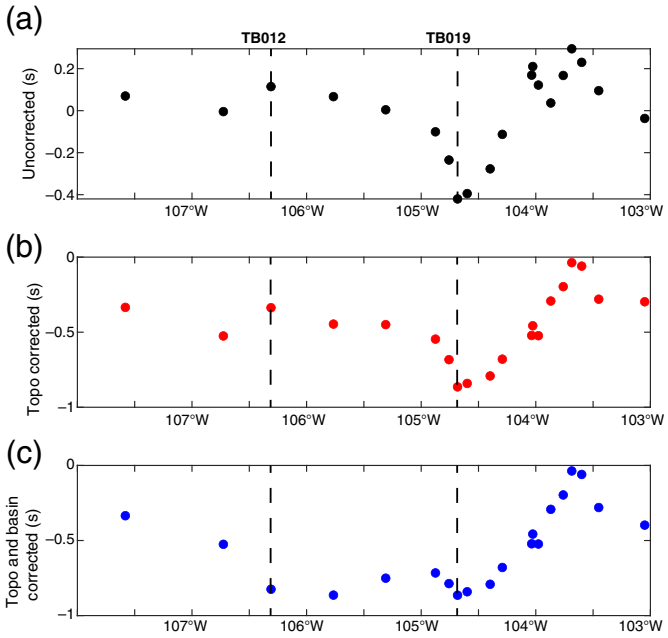

Figure 10. Mean *P*-wave delays for 26 teleseismic events recorded by the CIELO array. (a) Raw mean delays, (b) delays after correcting for elevation, and (c) delays after correcting for elevation and basin structure. The locations of stations TB012 and TB019 in the western and eastern edges of the basin, respectively, are shown for reference. The color version of this figure is available only in the electronic edition.

The presence of basin structure has several implications for our analysis of crust and mantle structure. For *Ps* receiver function analysis, basin multiples can interfere with the arrival of the direct *Ps* phase from the Moho (Yeck *et al.*, 2013), which is used in determination of crustal thicknesses. Despite these complications, there is a positive phase at several of the basin stations (Fig. 9) that is a plausible candidate for a Moho phase. The phase arrives earliest at station TB019 (~4.8 s) and arrives progressively later at stations to the west, reaching a maximum of ~6.8 s at station TB013. Although this phase is currently assumed to be the Moho phase, further work is needed to confirm its origin. Basin structure also affects teleseismic travel-time delays. To avoid contamination of the inverted mantle structure by these crustal delays, the basin structure must be accounted for. Figure 10 shows that, after correcting for topography, mean teleseismic *P* arrivals within the basin (between stations TB012 and TB019) occur slightly later than directly outside the basin. After correcting for travel time within the basin (using basin thickness values from Blackstone, 1993 and a mean basin V_P of 3000 km/s), these arrivals occur earlier than outside the basin, reflecting the high-velocity structure in the mantle.

Education and Outreach Activities

In addition to providing new constraints on the seismic structure of the Wyoming craton, the CIELO seismic experiment also provided numerous opportunities for education and outreach. Site TB037 was installed near the Hereford Country School, providing an excellent educational opportunity. This site was sufficiently accessible for elementary age students to visit, but remote enough to constitute an engaging field trip. Students from elementary to middle school age participated in both the installation and recovery of the station along with demonstrations of how seismic waves propagate, what can be learned about Earth from seismology, and the remarkable sensitivity of modern seismic instruments to seemingly weak sources of ground motion. During two trips to service the instruments, members of the servicing team visited the school to discuss earthquakes around the globe and what we might be able to record with the instrument the students helped install. Students and faculty from the Oglala Lakota College also assisted with the installation of site TB036, a significantly more remote location than site TB037 that was not accessible to elementary-aged students.

Summary

The CIELO seismic experiment was designed to provide high-resolution constraints on the seismic structure of the eastern half of the crust and lithosphere of the Wyoming craton to improve our understanding of the tectonic history of the region. Through combined analysis of shear-wave splitting, *Ps*- and *Sp*-receiver function analysis, attenuation, and body-wave tomography (among other possible analyses), we hope to (1) determine whether the Thunder Basin Block represents a stable, rigid block or delaminating lithosphere; (2) explore the relationship of the Thunder Basin Block relative to the Black Hills; and (3) place firmer constraints on the eastern boundary of the craton. In addition to outlining the purpose of the completed study and providing a description of preliminary results, this report provides a detailed discussion of data quality and availability. Future users of CIELO data (network 2F) should be aware of orientation issues and make corrections as needed. Future users should also take note of the anthropogenic noise present at stations such as TB015, as well as the presence of seasonal variations in long-period noise on the horizontal components of some stations.

Data and Resources

Seismic data collected as part of the Crust and lithosphere Investigation of the Easternmost expression of the Laramide Orogeny (CIELO) seismic experiment (and used in this study) have been archived at the Incorporated Research Institutions for Seismology Data Management Center (IRIS-DMC) at www.iris.edu (last accessed May 2021) under the network code 2F (https://doi.org/10.7914/SN/2F_2017). The data are restricted until December 2022. Data used in the discussion of sensor orientations, data completeness, power spectral density (PSD), and probability density functions (PDFs) are unrestricted and were obtained from IRIS Latest Assessment of Seismic Station Observations (LASSO) at http://lasso.iris.edu/ (last accessed May 2021) and IRIS Modular Utility for

STAtistical kNowledge Gathering system (MUSTANG) at http://services.iris.edu/mustang/ (last accessed May 2021). Event data were downloaded from the U.S. Geological Survey (USGS) Earthquake Catalog at https://earthquake.usgs.gov/earthquakes/search/ (last accessed May 2021). Previously published shear-wave splitting results were downloaded from the SPUD database at http://ds.iris.edu/spud/swsmeasurement (last accessed June 2021). The supplemental material file associated with this article includes three additional figures and associated captions.

Declaration of Competing Interests

The authors acknowledge that there are no conflicts of interest recorded.

Acknowledgments

The authors would like to begin by thanking the people who made this experiment possible, including the numerous landowners who generously provided access to their property during the duration of the two-year experiment, graduate students Gillian Goldhagen and Matthew Mendoza, and a number of dedicated undergraduates (Madeline Churchill, Austin Fimbres, Alan Horton, Jose Lara, Chelsea McCormick, Maxim Shapovalov, David Small, and John Wright) who assisted in installation, service runs, and station removal. The authors would also like to thank the Dakota Water Science Center in Rapid City, South Dakota, and Beth Wisely from Casper College for offering logistical support, the Incorporated Research Institutions for Seismology—Portable Array Seismic Studies of the Continental Lithosphere (IRIS-PASSCAL) Instrument Center for providing power related instrumentation, and Tim Parker (Nanometrics) for training and assistance in the field. The authors would also like to acknowledge the opportunity to work with Hannan Lagarry from Oglala Lakota College as well as the parents, teachers, and students from Hereford Elementary School (K-8) on outreach activities. The authors would also like to thank Kevin Ward and one anonymous reviewer for their helpful comments and suggestions. This work was supported by University of California, Riverside Regents Faculty Fellowship and a Grant in Aid from the University of Minnesota (proposal number 325013). The facilities of the IRIS Consortium are supported by National Science Foundation (NSF) Seismological Facilities for the Advancement of Geoscience (SAGE) Award, Cooperative Support Agreement EAR-1851048.

References

Anderson, M. L., R. C. Porter, W. L. Yeck, A. F. Sheehan, S. L. Beck, and H. J. Gilbert (2014). Contrasting lithospheres: Does one size fit all for the structure of mantle under foreland arches? *AGU Fall Meeting Abstracts*, T23A-4639, San Francisco, California, 15–19 December.

Bedle, H., C. M. Cooper, and C. D. Frost (2021). Nature versus Nurture: Preservation and destruction of Archean cratons, *Earth Space Sci. Open Arch.* doi: 10.1002/essoar.10506070.1.

Bezada, M. J. (2017). Insights into the lithospheric architecture of Iberia and Morocco from teleseismic body-wave attenuation, *Earth Planet. Sci. Lett.* **478,** 14–26.

Bezada, M. J., and J. Smale (2019). Lateral variations in lithospheric mantle structure control the location of intracontinental seismicity in Australia, *Geophys. Res. Lett.* **46,** no. 22, 12,862–12,869.

Bezada, M. J., J. Byrnes, and Z. Eilon (2019). On the robustness of attenuation measurements on teleseismic P waves: Insights from micro-array analysis of the 2017 North Korean nuclear test, *Geophys. J. Int.* **218,** no. 1, 573–585.

Bird, P. (1998). Kinematic history of the Laramide orogeny in latitudes 35–49 N, western United States, *Tectonics* **17,** no. 5, 780–801.

Blackstone, D. L. (1993). *Precambrian Basement Map of Wyoming—Outcrop and Structural Configuration*, Geological Survey of Wyoming [Wyoming State Geological Survey], Map Series 43, scale 1:1,000,000.

Bowman, J. R., and M. Ando (1987). Shear-wave splitting in the upper-mantle wedge above the Tonga subduction zone, *Geophys. J. Int.* **88,** no. 1, 25–41.

Clouzet, P., Y. Masson, and B. Romanowicz (2018). Box tomography: First application to the imaging of upper-mantle shear velocity and radial anisotropy structure beneath the North American continent, *Geophys. J. Int.* **213,** no. 3, 1849–1875.

Dave, R., and A. Li (2016). Destruction of the Wyoming Craton: Seismic evidence and geodynamic processes, *Geology* **44,** no. 11, 883–886.

Humphreys, E. D., B. Schmandt, M. J. Bezada, and J. Perry-Houts (2015). Recent craton growth by slab stacking beneath Wyoming, *Earth Planet. Sci. Lett.* **429,** 170–180.

Jordan, T. H. (1978). Composition and development of the continental tectosphere, *Nature* **274,** no. 5671, 544–548.

Kilian, T. M., K. R. Chamberlain, D. A. Evans, W. Bleeker, and B. L. Cousens (2016). Wyoming on the run—Toward final Paleoproterozoic assembly of Laurentia, *Geology* **44,** no. 10, 863–866.

Lee, C. (2006). Geochemical/petrologic constraints on the origin of cratonic mantle, *American Geophysical Monograph*, **164**, 89.

Mandic, V., V. C. Tsai, G. L. Pavlis, T. Prestegard, D. C. Bowden, P. Meyers, and R. Caton (2018). A 3D broadband seismometer array experiment at the homestake mine, *Seismol. Res. Lett.* **89,** no. 6, 2420–2429.

McNamara, D. E., and R. P. Buland (2004). Ambient noise levels in the continental United States, *Bull. Seismol. Soc. Am.* **94,** no. 4, 1517–1527.

Mueller, P. A., and C. D. Frost (2006). The Wyoming Province: A distinctive Archean craton in Laurentian North America, *Can. J. Earth Sci.* **43,** no. 10, 1391–1397.

O'Rourke, C. T., A. F. Sheehan, E. A. Erslev, and M. L. Anderson (2016). Small-magnitude earthquakes in north-central Wyoming recorded during the Bighorn Arch seismic experiment, *Bull. Seismol. Soc. Am.* **106,** no. 1, 281–288.

Peterson, J. (1993). Observations and modeling of seismic background noise, *U.S. Geol. Surv. Tech. Rept. 93-322*, 1–95.

Pollack, H. N. (1986). Cratonization and thermal evolution of the mantle, *Earth Planet. Sci. Lett.* **80,** nos. 1/2, 175–182.

Schmandt, B., and E. Humphreys (2010). Complex subduction and small-scale convection revealed by body-wave tomography of the western United States upper mantle, *Earth Planet. Sci. Lett.* **297,** nos. 3/4, 435–445.

Schmandt, B., and F. C. Lin (2014). P and S wave tomography of the mantle beneath the United States, *Geophys. Res. Lett.* **41,** no. 18, 6342–6349.

Stachnik, J. C., A. F. Sheehan, D. W. Zietlow, Z. Yang, J. Collins, and A. Ferris (2012). Determination of New Zealand ocean bottom

seismometer orientation via Rayleigh-wave polarization, *Seismol. Res. Lett.* **83,** no. 4, 704–713.

Tape, C., D. Christensen, M. M. Moore-Driskell, J. Sweet, and K. Smith (2017). Southern Alaska Lithosphere and Mantle Observation Network (SALMON): A seismic experiment covering the active arc by road, boat, plane, and helicopter, *Seismol. Res. Lett.* **88,** no. 4, 1185–1202.

Tikoff, B., and J. Maxson (2001). Lithospheric buckling of the Laramide foreland during Late Cretaceous and Paleogene, Western United States, *Rocky Mt. Geol.* **36,** no. 1, 13–35.

Wang, X., D. Zhao, and J. Li (2016). The 2013 Wyoming upper mantle earthquakes: Tomography and tectonic implications, *J. Geophys. Res.* **121,** no. 9, 6797–6808.

Whitmeyer, S. J., and K. E. Karlstrom (2007). Tectonic model for the Proterozoic growth of North America, *Geosphere* **3,** no. 4, 220–259.

Wolin, E., S. van der Lee, T. A. Bollmann, D. A. Wiens, J. Revenaugh, F. A. Darbyshire, A. W. Frederiksen, S. Stein, and M. E. Wysession (2015). Seasonal and diurnal variations in long-period noise at SPREE stations: The influence of soil characteristics on shallow stations' performance, *Bull. Seismol. Soc. Am.* **105,** no. 5, 2433–2452.

Worthington, L. L., K. C. Miller, E. A. Erslev, M. L. Anderson, K. R. Chamberlain, A. F. Sheehan, W. L. Yeck, S. H. Harder, and C. S. Siddoway (2016). Crustal structure of the Bighorn Mountains region: Precambrian influence on Laramide shortening and uplift in north-central Wyoming, *Tectonics* **35,** no. 1, 208–236.

Wüstefeld, A., G. Bokelmann, C. Zaroli, and G. Barruol (2008). SplitLab: A shear-wave splitting environment in Matlab, *Comput. Geosci.* **34,** no. 5, 515–528.

Yeck, W. L., A. F. Sheehan, and V. Schulte-Pelkum (2013). Sequential H-κ stacking to obtain accurate crustal thicknesses beneath sedimentary basins, *Bull. Seismol. Soc. Am.* **103,** no. 3, 2142–2150.

Zhu, Z., M. Bezada, J. S. Byrnes, and H. A. Ford (2020). Investigating the role of lithospheric heterogeneity in localizing deformation during the Laramide Orogeny: Insights from seismic attenuation, *AGU Fall Meeting 2020*, 1–17 December.

Manuscript received 24 August 2021
Published online 24 November 2021